Geophysical Journal International

Geophys. J. Int. (2021) **226,** 47–55
Advance Access publication 2021 March 08
GJI Seismology

doi: 10.1093/gji/ggab092

Joint inversion for 1-D crustal seismic *S*- and *P*-wave velocity structures with interfaces and its application to the Wabash Valley Seismic Zone

Yuchen Liu[*] and Lupei Zhu

Department of Earth and Atmospheric Sciences, Saint Louis University, St. Louis, MO 63108*, USA. E-mail:* lupei.zhu@slu.edu

Accepted 2021 March 1. Received 2021 January 20; in original form 2020 July 13

SUMMARY

Interfaces are important part of Earth's layering structure. Here, we developed a new model parametrization and iterative linearized inversion method that determines 1-D crustal velocity structure using surface wave dispersion, teleseismic *P*-wave receiver functions and *Ps* and *PmP* traveltimes. Unlike previous joint inversion methods, the new model parametrization includes interface depths and layer *Vp*/*Vs* ratios so that smoothness constraint can be conveniently applied to velocities of individual layers without affecting the velocity discontinuity across the interfaces. It also allows adding interface-related observation such as traveltimes of *Ps* and *PmP* in the joint inversion to eliminate the trade-off between interface depth and *Vp*/*Vs* ratio and therefore to reduce the uncertainties of results. Numerical tests show that the method is computationally efficient and the inversion results are robust and independent of the initial model. Application of the method to a dense linear array across the Wabash Valley Seismic Zone (WVSZ) produced a high-resolution crustal image in this seismically active region. The results show a 51–55-km-thick crust with a mid-crustal interface at 14–17 km. The crustal *Vp*/*Vs* ratio varies from 1.69 to 1.90. There are three pillow-like, ∼100 km apart high-velocity bodies sitting at the base of the crust and directly above each of them are a low-velocity anomaly in the middle crust and a high-velocity anomaly in the upper crust. They are interpreted to be produced by mantle magmatic intrusions and remelting during rifting events in the end of the Precambrian. The current diffuse seismicity in the WVSZ might be rooted in this ancient distributed rifting structure.

Key words: Composition and structure of the continental crust; Inverse theory; Joint inversion; Crustal imaging; Crustal structure.

1 INTRODUCTION

Earth has a layered structure as the result of gravitational differentiation throughout its evolution. Material properties such as density and seismic velocities are generally continuous within each layer but change abruptly at the layer boundaries (interfaces). For example, the Moho discontinuity is caused by a composition change from mafic rocks in the lower crust to peridotite in the mantle. The less pronounced Conrad discontinuity of continental crust is believed to correspond to a sharp transition from the felsic upper crust to the mafic lower crust. Such 1-D layered models are, of course, approximation of the real Earth structure that also varies laterally, but they are useful for constructing localized models. Because the seismic velocities and interface depths are functions of material chemical composition, pressure, temperature and deformation history, determining crust's layering structure using seismic observation at the surface gives us a way to probe its current status and to decipher its tectonic evolution.

Seismologists have been using seismic waveforms from earthquakes to study crustal velocity structure by inverting surface wave dispersion data (e.g. McEvilly 1964) and teleseismic *P*-wave receiver functions (RFs, e.g. Langston 1979; Owens *et al.* 1984). Surface wave dispersion data are sensitive to the average *S*-wave velocity to certain depth dependent of the period but insensitive to velocity jumps (e.g. Chang *et al.* 2004; Yoo *et al.* 2007). On the other hand, RFs are sensitive to *S*-wave velocity contrasts of interfaces but insensitive to the background crustal velocities (Ammon *et al.* 1990). The complementary nature of the two data sets led to the development of joint inversion methods (e.g. Last *et al.* 1997; Özalaybey *et al.* 1997; Julia *et al.* 2000). Studies have shown that joint inversion of the two data sets can significantly reduce the non-uniqueness of the solution and improve the resolution of the

---

[*] Now at: CGG, Houston, TX, USA.

velocity structure (e.g. Julià *et al.* 2003; Chang & Baag 2005; Shen *et al.* 2012). With the increasing number of global broad-band seismic stations and amount of surface wave dispersion measurements through ambient noise cross-correlation, joint inversion methods have been widely used for studying crustal structure in different geological regions (e.g. Du & Foulger 1999; Julià *et al.* 2005; Horspool *et al.* 2006; Tokam *et al.* 2010; Gilligan *et al.* 2014).

There are, however, several shortcomings in the current joint inversion methods. First, most of these methods invert for the *S*-wave velocities only because both the surface wave dispersion and RFs are mostly sensitive to the *S*-wave velocity structure. The *P*-wave velocities are determined by fixing the *Vp*/*Vs* ratio. The *Vp*/*Vs* ratio which is directly linked to the Poisson's ratio of material is, however, an important material property. Rocks with a similar *Vp* or *Vs* often have different *Vp*/*Vs* ratios. Thus, it is desirable to obtain both *P*- and *S*-wave velocities. Secondly, most joint inversion methods do not include interfaces in the model parameters. The smoothness constraint in these inversion methods tends to produce a gradual variation of velocity with depth without any velocity jumps. Important interfaces such as the Moho have to be picked *posteriorly* from the obtained velocity model using certain *ad hoc* criteria (e.g. Horspool *et al.* 2006; Yoo *et al.* 2007; Gilligan *et al.* 2014; Ammirati *et al.* 2015; Bao *et al.* 2015). There are a few joint inversion methods that include interface depth as a model parameter (e.g. Sambridge 1999; Xu *et al.* 2013); however, they use non-linear inversion algorithms which usually limit the total number of model parameters and are time consuming. Thirdly, without interfaces in the model, it is not possible to add interface-related data such as the *Pn* station delays and Moho reflected *P* waves (*PmP*) traveltimes to the joint inversion. These types of data are crucial for constraining the *P*-wave velocities and the *Vp*/*Vs* ratios.

In this study, we developed a new linearized joint inversion method to determine 1-D crustal *S*-wave velocities, *Vp*/*Vs* ratios, and interface depths simultaneously using surface wave dispersion, RFs, and interface-related traveltimes of *P*-to-*S* converted waves (*Ps*) and *PmP*. The newly added traveltime data are sensitive to the interface depths and crustal *P*-wave velocities and, therefore, can help to constrain these parameters. We tested the new method using synthetic data and then applied it to a dense linear array across the Wabash Valley Seismic Zone (WVSZ) to obtain a high-resolution crustal velocity structure profile in the region. We compared the results to velocity structures from previous studies and discuss the advantages of the method in the end.

2 METHODOLOGY

For an arbitrary 1-D velocity model of L layers with smooth variation of velocity in each layer (Fig. 1), we used the layer *S*-wave velocities, thickness H, and *Vp*/*Vs* ratio κ as the model parameters. We divided each layer i into a number (n_i) of thin sublayers so that the *S*-wave velocity in each sublayer β_{ij} is constant. The density of each sublayer was determined from the *P*-wave velocity $\alpha_{ij} = \kappa_i \beta_{ij}$ using the empirical relationship $\rho_{ij} = 0.32\alpha_{ij} + 0.77$ (Berteussen 1977). The model vector $\mathbf{m}$ is arranged as

$$\mathbf{m} = [\mathbf{V}, \mathbf{H}, \kappa]^{\mathrm{T}}, \tag{1}$$

where

$$\mathbf{V} = [\beta_{11}, \ldots, \beta_{1n_1}, \beta_{21}, \ldots, \beta_{Ln_L}]^{\mathrm{T}}, \tag{2}$$

$$\mathbf{H} = [H_1, H_2, \ldots, H_{L-1}]^{\mathrm{T}}, \tag{3}$$

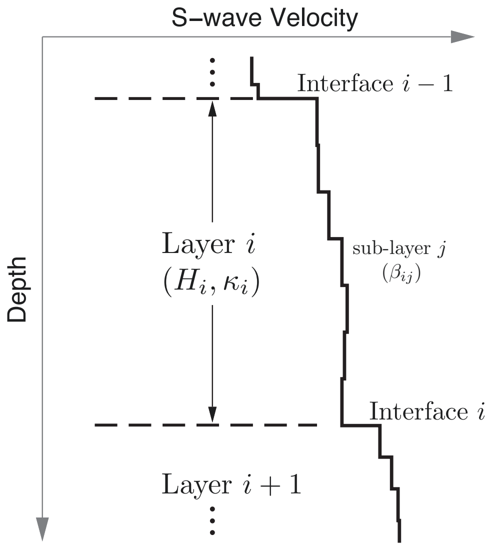

Figure 1. Velocity model parametrization.

$$\kappa = [\kappa_1, \kappa_2, \ldots, \kappa_L]^{\mathrm{T}}, \tag{4}$$

T denotes the transpose.

The data vector $\mathbf{d}$ in the new joint inversion method contains four types of data: surface wave dispersion measurements $\mathbf{d}^{(1)}$, RF waveform time series $\mathbf{d}^{(2)}$, *Ps* delay times $\mathbf{d}^{(3)}$ from different interfaces and *PmP* traveltime $\mathbf{d}^{(4)}$. They are related to the model through a set of non-linear functions:

$$\mathbf{d} = \mathbf{f}(\mathbf{m}). \tag{5}$$

Surface wave dispersion and RFs of 1-D layered model can be calculated using the propagator matrix method (Haskell 1964). Equations for calculating t_{Ps} and t_{PmP} are given in the Appendix.

We sought the optimal model that minimizes a weighted sum of L_2 norm squares of the prediction errors of the four data types:

$$\chi^2 = \sum_{i=1}^{4} \frac{N_i'}{N_i} \frac{\|\mathbf{d}^{(i)} - \mathbf{f}^{(i)}(\mathbf{m})\|^2}{\sigma_i^2}, \tag{6}$$

where N_i is the number of data points in data set i, $N_i' \leq N_i$ is the number of independent data points (N_i' is estimated based on the data bandwidth and sampling intervals, as shown later) and σ_i is data's standard deviation. The solution can be obtained by linearizing eq. (5) at an initial model $\mathbf{m}_0$,

$$\mathbf{WGm} = \mathbf{W}(\mathbf{d} - \mathbf{d}_0 + \mathbf{Gm}_0), \tag{7}$$

where $\mathbf{G}$ is the partial derivative matrix of $\mathbf{f}$ with respect to the model and $\mathbf{d}_0 = \mathbf{f}(\mathbf{m}_0)$. The weighting matrix $\mathbf{W}$ for data type i is

$$W_{jk}^{(i)} = \frac{1}{\sigma_i} \sqrt{\frac{N_i'}{N_i}} \delta_{jk}, \tag{8}$$

where δ_{jk} is the Kronecker delta.

We added smoothness and damping constraints on the model parameters:

$$\mathbf{Lm} = \mathbf{0}, \tag{9}$$

$$\lambda\mathbf{m} = \lambda\mathbf{m}_0. \tag{10}$$

Table 1. Comparison of interface depth z in km and layer Vp/Vs ratio κ of the true model and models from joint inversion of the noise-free and noise-added synthetic data (the last three columns). SW, surface wave dispersion data; RF, receiver function waveform data; Ps, *Ps* delay time data; All, all three types plus the *PmP* traveltime.

	True	Noise-free	SW+RF	SW+RF+Ps	All data
χ^2		0.02	0.94 ± 0.04	0.93 ± 0.04	0.93 ± 0.04
z_1	1.0	1.8 ± 0.1	1.4 ± 0.4	1.4 ± 0.4	1.3 ± 0.4
κ_1	1.90	1.85 ± 0.06	1.87 ± 0.07	1.88 ± 0.07	1.88 ± 0.06
z_2	15.0	15.2 ± 0.3	16.7 ± 2.6	15.8 ± 1.6	15.6 ± 1.3
κ_2	1.78	1.78 ± 0.02	1.78 ± 0.04	1.77 ± 0.04	1.78 ± 0.02
z_3	39.0	38.5 ± 1.3	41.6 ± 3.2	39.8 ± 1.9	39.2 ± 1.5
κ_3	1.78	1.78 ± 0.02	1.78 ± 0.04	1.77 ± 0.04	1.78 ± 0.02
z_4	45.0	45.1 ± 1.9	47.0 ± 3.1	45.7 ± 2.1	45.0 ± 1.3
κ_4	1.78	1.78 ± 0.02	1.78 ± 0.04	1.77 ± 0.04	1.78 ± 0.02
κ_5	1.75	1.75 ± 0.01	1.75 ± 0.01	1.75 ± 0.01	1.75 ± 0.01

Specifically, the smoothness constraint for *S*-wave velocity of sub-layer *j* in layer *i*,

$$a_i(\beta_{ij-1} - 2\beta_{ij} + \beta_{ij+1}) = 0, \tag{11}$$

and for Vp/Vs ratios of neighboring layers,

$$b_i(\kappa_i - \kappa_{i+1}) = 0, \tag{12}$$

where a_i and b_i are smoothness weights for the layer.

We also added inequality constraints

$$\mathbf{Hm} \geq \mathbf{h}, \tag{13}$$

to require that the layer thicknesses are positive and the Vp/Vs ratios are within certain specified range. Optionally, for the Moho and those interfaces with *Ps* phases observed, one may also require the velocity jump across the interface larger than certain threshold.

Eqs (7), (9), (10) and (13) can be solved together for $\mathbf{m}$ using the least-squares principle with inequality constraints (e.g. Lawson & Hanson 1974; Menke 2012). The process is then repeated using $\mathbf{m}$ as the new initial model vector until the misfit χ^2 is less than a threshold or the number of iterations exceeds a preset limit. The uncertainty of the final model can be estimated using the model covariance matrix

$$\mathrm{cov}(\mathbf{m}) = \mathbf{M}\mathrm{cov}(\mathbf{d})\mathbf{M}^{\mathrm{T}}, \tag{14}$$

where $\mathrm{cov}(\mathbf{d})$ is the data covariance matrix and

$$\mathbf{M} = \left((\mathbf{WG})^{\mathrm{T}}(\mathbf{WG}) + \mathbf{L}^{\mathrm{T}}\mathbf{L} + \lambda^2\mathbf{I}\right)^{-1}(\mathbf{WG})^{\mathrm{T}}\mathbf{W}. \tag{15}$$

It should be pointed out that the above uncertainty estimation is based on the linear approximation and only works when the inverse problem is not too non-linear (Lai *et al.* 2005). In general, for non-linear inverse problem, the Gaussian-distributed data errors are mapped into non-Gaussian distributed model parameter uncertainties (Menke 2012). Other techniques such as the boot-strapping method can be used to get more reliable model uncertainty estimates.

3 NUMERICAL TESTS

We conducted numerical tests using synthetic data to demonstrate the correctness of the new method and its improvements over previous joint inversion methods. The true velocity model consists of a sedimentary layer, the upper crust, the lower crust and the mantle (Table 1 and Fig. 2). There is a broad low velocity zone in the middle of the lower crust and a thin high velocity layer at the base of the lower crust (the basal layer). We used Computer Programs in Seismology (Herrmann 2013) to calculate RF and surface wave dispersion 'data'. The RF was computed using a ray parameter of 0.06 s km^{-1} and low-pass filtered with a Gaussian filter of $\alpha = 3.0$ s^{-1} (∼1 Hz corner frequency). The surface wave dispersion data were generated at 72 periods logarithmically evenly-spaced from 1.5 to 80 s. The *PmP* traveltime was calculated using eq. (A2) with a ray parameter of 0.10 s km^{-1}. The *Ps* delay times from the mid-crust interface, the top of basal layer and the Moho were calculated using eq. (A1) using a ray parameter of 0.06 s km^{-1}. We did not use the *Ps* delay time from the sediment-basement interface because it is usually not easy to pick it in real data.

We first tested our joint inversion method using the noise-free synthetic data. We used the first 11 s of RF waveform in the inversion to exclude the crustal multiples of Moho *Ps*. Since the RF was low-pass filtered at 1 Hz, we counted each period (1 s) of waveform segment as one independent data point. For the dispersion data, we counted every three neighboring measurements as one independent data based on the sampling interval and sensitivity kernels of surface wave dispersion. During the inversion, we required the Vp/Vs ratios to be between 1.5 and 2.0 and the *S*-wave velocity jumps across all interfaces to be larger than 0.1 km s^{-1}. The results after 15 iterations are listed in Table 1 and shown in Fig. 2. The uncertainties of model parameters were estimated using eq. (14) and assuming a σ_d of 0.03 for the RF waveform, 0.2 s for the *Ps* times and 0.4 s for the *PmP* time. The dispersion data standard deviations are 2 per cent for the phase velocities and twice as much for the group velocities, which is in general the case for real data. The results show that starting from an arbitrary five-layer model, the inversion fully recovered the true velocity model in terms of the layer velocities, Vp/Vs ratios, and interface depths except the sedimentary layer (Fig. 2). The overestimated thickness and underestimated Vp/Vs ratio of the sedimentary layer are not surprising as we did not have the *Ps* time delay from its bottom interface. The surface wave dispersion data and low-pass filtered RF waveform do not have the resolving power of the thin sedimentary layer.

To find the effects of data noise and initial velocity model on the inversion results, we conducted four more tests using randomly generated initial models and noise-added synthetic data. Gaussian-distributed noises were generated using the standard deviations specified above and were added to the synthetic data. In the first noisy data test, we used a one-layer model without interface and only the surface wave dispersion and RF waveform data. This was to simulate the previous joint inversion technique. We repeated the inversion 100 times using randomly generated initial models and noise-added data. Fig. 3 show the averages and estimated standard deviations of obtained model parameters. Fits to the noise-added data of all 100 final models are good as demonstrated by the final χ^2 values of 1.00 ± 0.03. All final *S*-wave velocity structure are in good agreement with the true model except that all velocity discontinuities in the true model become gradational because of the smoothness constraint. The true Vp/Vs ratio (1.78 in the crust) was not well recovered by the inversion. The Vp/Vs ratios of 100 final models have a mean of 1.81 with a standard deviation of 0.03. This confirmed that the surface wave dispersion and RF data only (without the crustal multiple converted phases) could not constrain the crustal Vp/Vs ratio.

Next, we repeated the above test but used a five-layer model with four interfaces. The inversion was repeated 100 times again using randomly generated initial models. The averages of model parameters and their estimated standard deviations are listed in Table 1 and are shown in Fig. 3. Even though the overall fitness

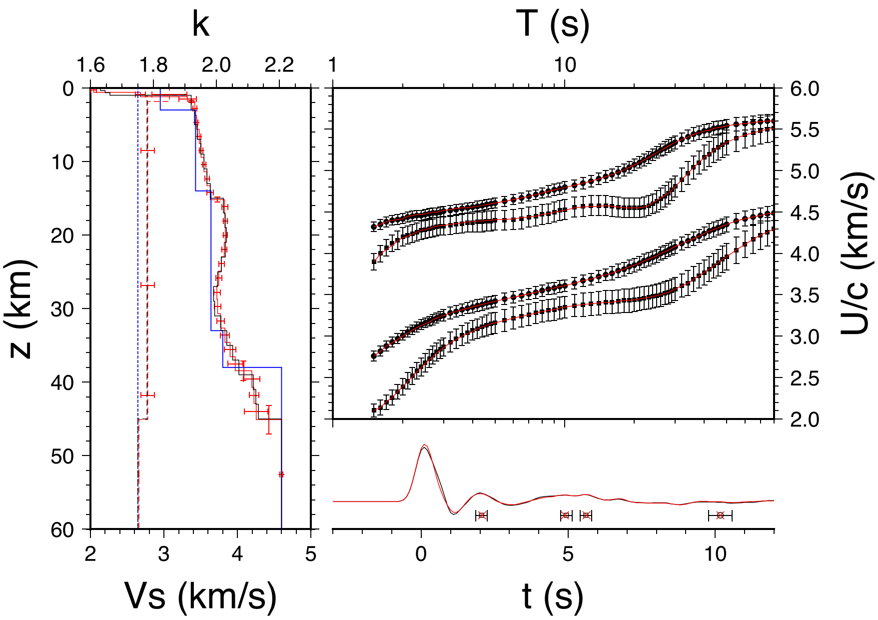

Figure 2. The black-coloured lines and symbols show the true velocity model of *S*-wave velocity and *Vp*/*Vs* ratio κ (left-hand panel) and its group (*U*, filled squares) and phase (*c*, filled circles) velocities of the Love and Rayleigh waves, receiver function, *Ps* times (open squares), and *PmP* traveltime (open circle). The Rayleigh wave velocities are shifted up by 1.5 km s^{-1} for displaying purpose. The blue-coloured lines show the initial velocity model for the joint inversion. The obtained velocity model with the standard deviations and its predicted surface wave dispersion, receiver function, *Ps* times and *PmP* traveltime are shown in red colour.

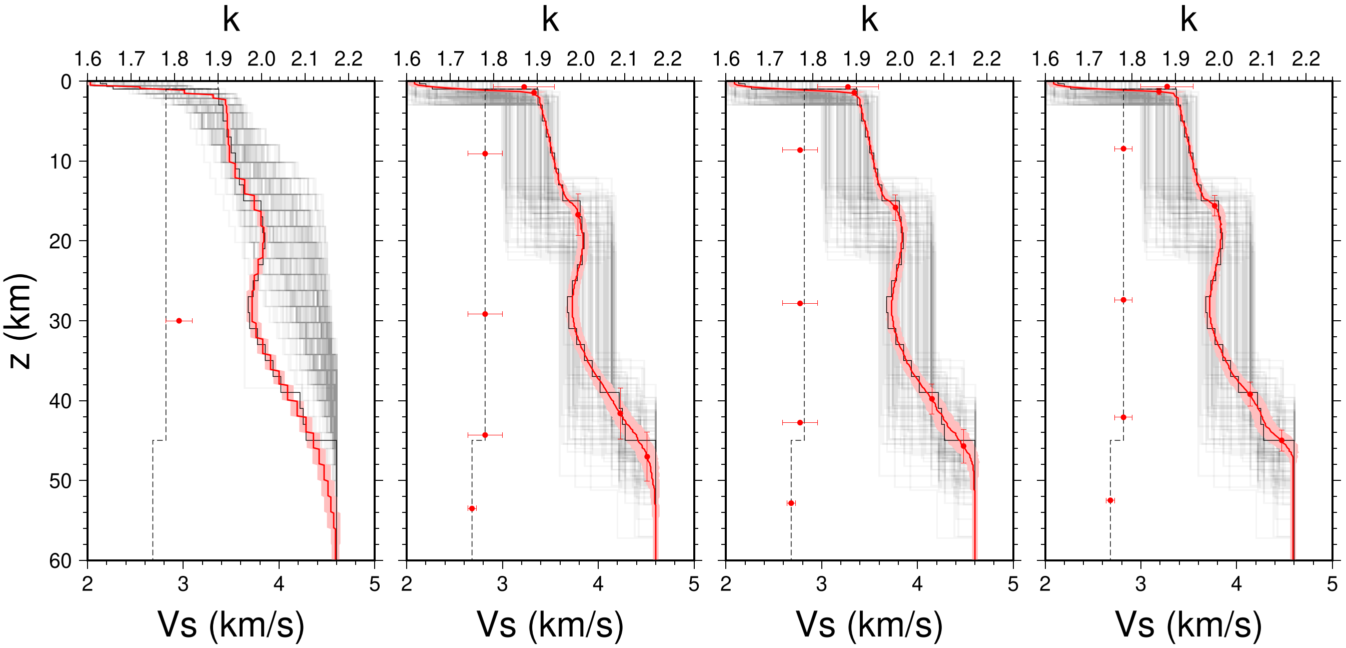

Figure 3. Velocity model results from 100 joint inversions of noise-added synthetic data and random initial models (grey lines), from left to right, (1) using one-layer models and surface wave dispersion plus receiver function waveform only, (2) using five-layer models and surface wave dispersion plus receiver function waveform only, (3) using five-layer models and surface wave dispersion plus receiver function waveform plus *Ps* times, (4) using five-layer models and surface wave dispersion plus receiver function waveform plus *Ps* times plus the *PmP* traveltime. Black-colour solid lines and dashed lines are *S*-wave velocity and *Vp*/*Vs* ratios of the true model, respectively. Red-colour solid lines with shades and symbols with error bars are the averaged *S*-wave velocities and *Vp*/*Vs* ratios with their standard deviations based on the 100 inversion results.

to the data as measured by χ^2 of 0.94 was improved by a small amount compared with the one-layer inversions, the joint inversions with interfaces in the model parameters produced final velocity models better resembling the true model. The depth of the sediment-basement interface is 1.4 ± 0.4 km, close to the true value (1 km). The estimated Moho depth is 47.0 ± 3.1 km (45 km of the true Moho depth), the top of the basal layer is 41.6 ± 3.2 km deep (39 km in the true model), and the Conrad depth is 16.7 ± 2.6 km (15 km in the true model).. The estimated crustal *Vp*/*Vs* ratio is 1.78 ± 0.04 (1.78 in the true model). Again, the large uncertainties

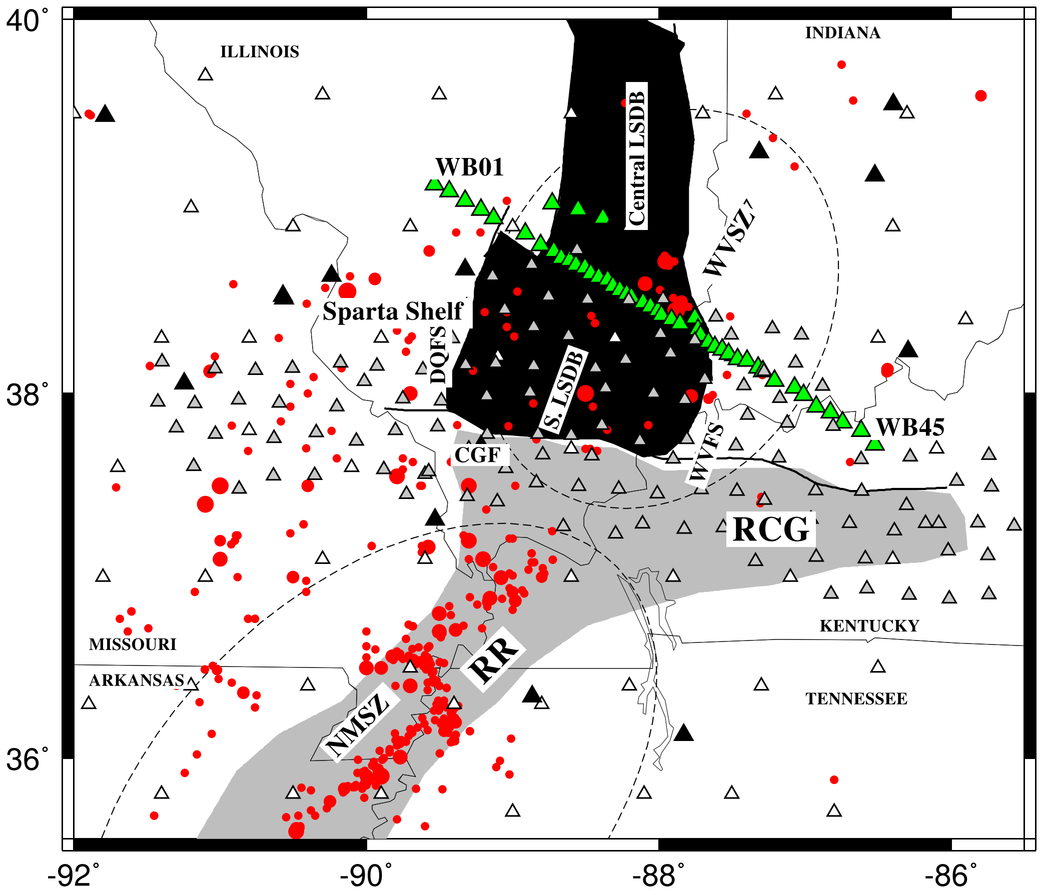

Figure 4. Simplified geology map of the New Madrid Seismic Zone (NMSZ) and Wabash Valley Seismic Zone (WVSZ), modified from Aziz Zanjani *et al.* (2019). The grey-coloured region shows the location of Reelfoot Rift (RR) and Rough-Creek Graben (RCG). Other acronyms are CGF (the Cottage Grove Fault), WVFS (the Wabash Valley Fault System), DQFS (the DuQuoin Fault System) and LSDB (the La Salle Deformation Belt). Green triangles are 47 seismic stations deployed during the 2014–2016 seismic recording experiment. Other triangles are temporary and permanent seismic stations in the area. Red dots are seismicity between 1962 and 2017 with the size proportional to the event magnitude.

in the interface depths and crustal *Vp*/*Vs* ratio are due to the lack of *P*-wave velocity sensitivity in the surface wave dispersion and RF data and the trade-off between the two model parameters.

We then repeated the five-layer joint inversion but added the observation of *Ps* times from the mid-crust interface and Moho. The results are listed in Table 1 and are shown in Fig. 3. The data fitness χ^2 of 0.93 was the about same as in the previous test but adding the *Ps* times helped to reduce the errors and uncertainties of the estimated discontinuity depths. There was no improvement to the crustal *Vp*/*Vs* ratio estimate, due to the fact that only surface wave dispersion and RF data were used.

Finally, we added the *PmP* traveltime data and repeated the test again. The results are also listed in Table 1 and shown in Fig. 3. There was no change to the data fitness, but including the *PmP* traveltime in the joint inversion reduced the uncertainties of interface depths and crustal *Vp*/*Vs* ratio. This is because the *PmP* traveltime helped to constrain the crustal *Vp*/*Vs* ratio which in turn helped to constrain the interface depths by eliminating the trade-off between the depth and *Vp*/*Vs* ratio. The averaged crustal *Vp*/*Vs* ratio and Moho depth matched the corresponding values of the true velocity model. It should be pointed out that the *PmP* traveltime only helped to constrain the average crustal *Vp*/*Vs* ratio and Moho depth. It did not help to improve the estimates of the sedimentary layer's *Vp*/*Vs* ratio and thickness and the mid-crust interface depth. The estimated standard deviations of model parameters using eq. (14) (in the 3rd column of Table 1) are close to the boot-strapping estimated values (in the last column of Table 1), except that the uncertainties of the sediment thickness and mid-crust depth using eq. (14) were underestimated.

4 APPLICATION TO THE WVSZ

We applied the newly developed joint inversion method to the WVSZ in the central U.S.A. The WVSZ is located in the southern Illinois and Indiana, north of the New Madrid Seismic Zone (NMSZ, Fig. 4). Similar to the NMSZ, which is famous for its intraplate seismicity and devastating 1811–1812 *M* 7 earthquakes (Nuttli 1973), the WVSZ is also characterized by relatively high seismicity. Liquefaction studies have demonstrated that several earthquakes with magnitudes larger than *M* 6.5 have occurred in the WVSZ during the past 12 000 yr (Pond & Martin 1997; Obermeier 1998). The largest earthquake in the WVSZ might have reached ∼*M* 7.5, as suggested by Obermeier (1998). Several moderate-sized earthquakes have been recorded in the WVSZ since the 1970s, which caused minor damage to the region (Stauder & Nuttli 1970; Hamburger & Rupp 1988; Kim 2003; Herrmann *et al.* 2008; Yang *et al.* 2009).

In order to reveal the crustal and upper mantle structure beneath the WVSZ and to shed lights on the intraplate seismicity mechanism in the region, researchers from Southern Illinois University

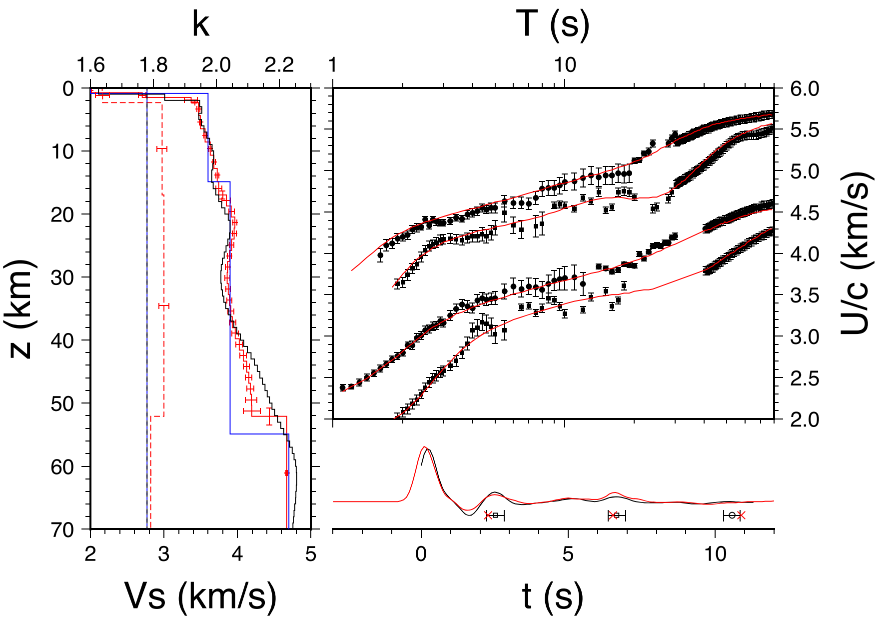

Figure 5. Inversion results at the centre ($x =$ km) of the profile. The left-hand panel shows the initial velocity model (blue, the solid lines are *S*-wave velocity V_s and the dashed lines are *Vp*/*Vs* ratio κ) and the final model (red) after 15 iterations. The black lines are the final velocity model obtained by Aziz Zanjani *et al.* (2019). The right-hand panel shows the observed group (*U*, filled squares) and phase (*c*, filled circles) velocities of the Love and Rayleigh waves, receiver function (the black-colour trace), *Ps* times (open squares), *PmP* traveltime (open circle) and the predictions (red) of the final model. The Rayleigh wave velocities are shifted up by 1.5 km s^{-1} for displaying purpose.

Carbondale (SIUC) and Saint Louis University (SLU) conducted a seismic recording experiment from 2014 to 2016 (Aziz Zanjani *et al.* 2019). Forty-four three-component broad-band seismographs were deployed as a 300-km-long linear array across the WVSZ, with a station spacing of 5 km in the middle and 10 km elsewhere (Fig. 4). Aziz Zanjani *et al.* (2019) did an ambient noise tomography of surface wave group and phase velocities between periods of 1 and 40 s along the linear array. They also calculated teleseismic *P* RFs of all stations and obtained a common-conversion-point (CCP) stacking image of RFs along the array. They then did joint inversion of surface wave dispersion and CCP-stacked RF for every 2-km-long segment of the 300-km-long profile. The results show a 50–60-km-thick crust that consists of a 1–3-km-thick sedimentary layer, a ∼15-km-thick upper crust, and a ∼30–40-km-thick lower crust. They found a high-velocity anomaly in the upper crust beneath the La Salle Deformation Belt (LSDB) and several high-velocity anomalies at the base of the lower crust, which they interpreted as high-density magmatic bodies produced by intrusion of mantle material during rifting events in the end of the Precambrian.

Aziz Zanjani *et al.* (2019) only determined *S*-wave velocities of the crust and uppermost mantle. The *Vp*/*Vs* ratio was fixed to 1.78. The interface depths were derived using their *Ps* delay times and the obtained *S*-wave velocity models. Because the crustal *P*-wave velocities were not constrained, the interface depths had large uncertainties due to the trade-off between depth and *Vp*/*Vs* ratio. To improve the results, we applied the newly developed joint inversion method to the same surface wave dispersion and RF data but added *Ps* delay times and *PmP* traveltime data. The *Ps* delay times of the Moho and mid-crust interfaces were picked in their CCP stacking image (fig. 2 in Aziz Zanjani *et al.* 2019). The uncertainty for *Ps* times was estimated to be 0.3 s. The *PmP* traveltimes were measured using teleseismic *S*-wave waveforms (Zhu & Liu 2020), with estimated uncertainties of 0.2–0.6 s.

Our starting model consists of a 1.5-km-thick sedimentary layer, a 14-km-thick upper crust, a 40-km-thick lower crust, and a half-space mantle (Fig. 5). The sedimentary layer was further divided into three sublayers of 0.5 km in thickness and the upper and lower crustal layers were divided into 2-km-thick sublayers. The iterative inversion terminated when the maximum number (15) of iterations was reached or the change of χ^2 was less than 0.001. Fig. 5 shows an example of inversion results at the centre of the profile ($x = 1$ km). The final velocity model has a sedimentary layer of 2.3 ± 0.1 km thick atop the upper crust of 14.7 ± 0.6 km thick. The Moho is at a depth of 52.1 ± 1.3 km. The *S*-wave velocity increases gradually from 3.5 km s^{-1} beneath the sedimentary layer to 3.9 km/s at the depth of 20 km. It stays nearly constant to 40 km depth then increases again to 4.2 km s^{-1} at the base of the crust. The crustal *Vp*/*Vs* ratio is 1.83 ± 0.02. The overall fit to the observation is good ($\chi^2 = 0.91$), with most predicted values within one standard deviation of the observation except some group velocity measurements between 5 and 30 s that differ from the prediction by more than two standard deviations. We noted that those group velocity measurements vary abruptly with period but have smaller standard deviations compared with their phase velocity counterparts. Usually the phase velocities are measured more accurately than the group velocities. It is likely that those group velocity uncertainties were underestimated in the surface wave tomography of previous study. Group velocities in this period range affect *S*-wave velocities between depths of 5 and 30 km. Fortunately, we had more accurate phase velocity measurements and the smoothness constraint in the joint inversion to mitigate the influence of group velocity measurement outliers. We compared our final model with that by Aziz Zanjani *et al.* (2019) using only the surface wave dispersion and RF waveform data (Fig. 5). The two models are similar, especially in the top 15 km. The largest difference is in the bottom of the lower crust where the *S*-wave velocity in their model increases gradually to the upper-mantle

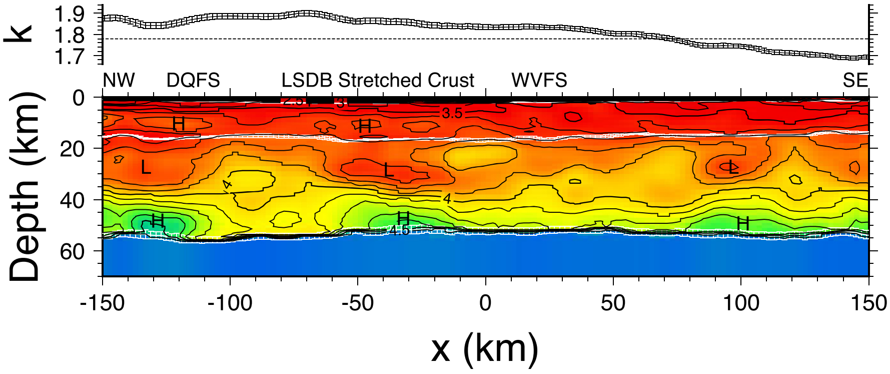

Figure 6. Variations of crustal Vp/Vs ratio κ (excluding the sedimentary basin) with error bars, *S*-wave velocity (shown in colours and contours at a contour interval of 0.1 km s^{-1}), and interface depth (white-coloured lines with error bars) along the linear array across the WVSZ. 'H' and 'L' shows high- and low-velocity anomalies in the upper and lower crust.

velocity due to the smoothness constraint and lack of interface in their joint inversion method.

For each segment of the profile we obtained one 1-D velocity model by following the above procedure and then stitched them together to form a 2-D crustal structure image of the profile. To make the image laterally smooth, we applied a five-point moving averaging to the velocity models. Fig. 6 shows the variation of *S*-wave velocity, interface depths and the crustal Vp/Vs ratio along the profile. Overall, the results are similar to those of Aziz Zanjani *et al.* (2019). The sedimentary layer thickness varies between 1.0 and 2.4 km, with the thickest beneath the LSDB in the middle part (x = –80 to 10 km) of the profile. The mid-crust interface is relatively flat between 14 and 17 km deep. The average Moho depth is 53 ± 1 km, with the shallowest (51 km) beneath the LSDB in the middle of the profile and the deepest (55 km) beneath the DuQuoin Fault System (DQFS, Fig. 6). The Moho topography is smoother and ~5 km shallower than in Aziz Zanjani *et al.* (2019). The difference is mostly due to the variation of crustal Vp/Vs ratio along the profile revealed by this study. The crustal Vp/Vs ratios are higher (1.84–1.90) in the NW than those (1.69–1.75) in the SW (Fig. 6), while the previous study fixed the Vp/Vs ratio at 1.78 (Aziz Zanjani *et al.* 2019). Several high- and low-velocity anomalies, labelled 'H' and 'L' in Fig. 6, are identified in the upper and lower crust. Most of these velocity anomalies were found in the previous results (fig. 7 in Aziz Zanjani *et al.* 2019), but the new results delineate them more clearly, especially the three pillow-like high velocity anomalies in the base of the crust.

Our crustal Vp/Vs ratios of 1.69–1.90 based on surface wave dispersion, RF, and *PmP* data agree with those by Ma & Lowry (1997) using RF and gravity data of USArray stations in our study region. The typical crustal Vp/Vs ratio is between 1.76 and 1.79 (Zandt & Ammon 1995). Higher values of 1.79–1.87 suggest more mafic composition (Christensen 1996). Aziz Zanjani *et al.* (2019) interpreted the two high-velocity anomalies at the base of the crust in the middle of the profile and to the SE as the so-called 'rift pillow' (Ervin & McGinnis 1975; Braile *et al.* 1986) or 'fossil rift cushion' (Mooney *et al.* 1983). They likely represent magmatic intrusions from the mantle during rifting events at the end of Precambrian. The low-velocity anomalies in the middle crust and the high-velocity anomalies in the upper crust above the pillows were interpreted as felsic-mafic igneous bodies derived from remelting and differentiation of the mantle intrusion. Our new image shows one more such intrusion and magmatic feature in the NW end of the profile (Fig. 6). It indicates that the Precambrian rifting beneath the WVSZ was not localized but occurred in several rifts separated by ~100 km. The larger sizes of velocity anomalies and higher Vp/Vs ratios in the NW side of the profile than in the SE side suggest that the rifting was heterogeneous with more magmatic intrusion volume in the NW side. The diffuse seismicity in the WVSZ may be related to the pre-existing broad rifting structure.

5 DISCUSSION AND CONCLUSIONS

Both the numerical tests and application to the WVSZ data show that adding interfaces as model parameters makes the model more realistic and helps to improve inversion results. The previous joint inversion methods without velocity interfaces produce artificially gradational Moho and other crustal interfaces because of the smoothness constraint to the velocity variation. Our new model parametrization allows us to apply the smoothness constraint to *S*-wave velocity variation within each layer and to add Vp/Vs ratios of different layers as model parameters. The benefits come at a cost of computation time increase of ~200 per cent for calculating the partial derivatives with respect to the interface depths and layer Vp/Vs ratios. The total computation time, however, is still affordable. It only takes 2–3 min to finish a joint inversion for a typical five-layer velocity model in a MacBook Pro laptop with a 2.4 GHz Intel Core i5 CPU.

The numerical tests and application also show that including layer Vp/Vs ratios helps to reduce the uncertainties of inversion results. Surface wave dispersion and RF data are mainly sensitive to the *S*-wave velocity structure. Unless there are clear crustal multiples of Moho *P*-to-*S* converted waves in the RFs, the crustal Vp/Vs ratio is not constrained. A lack of Vp/Vs ratio constraint leads to lack of constraint on the crustal thickness (Zhu & Kanamori 2000), which, in turn, leads to uncertainty in the obtained crustal *S*-wave velocities because of the trade-off between crustal velocity and thickness in the data. Adding the *PmP* traveltime data in the inversion in this case played an important role in constraining the crustal Vp/Vs ratio and reducing the standard deviations of Moho depth and crustal velocities.

There are several aspects of the new joint inversion method that can be improved in the future. The current implementation uses the traveltime of post-critical Moho reflection *PmP* to help to constrain the crustal Vp/Vs ratio. Post-critical *PmP* travels in the crust for ~100 km horizontally thus its lateral resolution power is limited. In addition, it can only help to constrain the Vp/Vs ratio of the whole crust and is unable to resolve Vp/Vs ratio variation between crustal layers. Data from near vertical *P*-wave reflection and conversion phases from different crustal interfaces would be more desirable. Another problem with the current approach of 1-D velocity inversion and stitching is that no *a priori* lateral smoothness constraint can be applied to the velocity model. Our current solution is to smooth the data laterally, for example, using dispersion data from surface wave tomography and CCP-stacked RFs, so that the obtained 1-D models are laterally smooth, provided that the inverse problem is not too non-linear. The final 2-D or 3-D velocity model can also be smoothed *posteriorly* using a multipoint moving averaging to remove possible vertical stripes in the final crustal structural image. In the future with more computation capacity, direct joint inversion for 2-D and 3-D models is feasible.

In summary, we developed a new model parametrization and iterative linearized inversion method that determines 1-D crustal velocity structure using surface wave dispersion, teleseismic *P*-wave RFs and *Ps* and *PmP* traveltimes. Unlike previous joint inversion methods, the new model parametrization includes interface depths and layer Vp/Vs ratios so that smoothness constraint can be conveniently applied to velocities of individual layers without affecting the velocity discontinuity across the interfaces. It also allows adding interface-related observation such as traveltimes of *Ps* and *PmP* in the joint inversion to eliminate the trade-off between interface depth and Vp/Vs ratio and therefore to reduce the uncertainties of results. Numerical tests show that the method is computationally efficient and the inversion results are robust and independent of the initial model. Application of the method to a dense linear array across the WVSZ produced a high-resolution crustal image in this seismically active region. The results show a 51–55-km-thick crust with a mid-crustal interface at 14–17 km. The crustal Vp/Vs ratio varies from 1.69 to 1.90. There are three pillow-like, ∼100 km apart high-velocity bodies sitting at the base of the crust, and directly above each of them are a low-velocity anomaly in the middle crust and a high-velocity anomaly in the upper crust. They are interpreted to be produced by mantle magmatic intrusions and remelting during rifting events in the end of the Precambrian. The current diffuse seismicity in the WVSZ might be rooted in this ancient distributed rifting structure.

ACKNOWLEDGEMENTS

We thank Asiye Aziz Zanjani for providing the Wabash Valley surface wave dispersion and receiver function data and Bob Herrmann for his Computer Programs in Seismology package. Comments from Linda Warren, Bob Herrmann, Walter Mooney and two anonymous reviewers helped us to improve the manuscript. The 2014-2016 Wabash Valley Seismic Recording Experiment was a USArray Flexible Array project (network code 6E) funded by NSF grands EAR-249577 (J.A. Conder at SIUC) and EAR-1249701 (L. Zhu at SLU). Waveform data of the experiment used in this study have been archived and available at the IRIS DMC (https://ds.iris.edu/ds/nodes/dmc/). The study was supported by NSF grants EAR-1249701 and EAR-1661519.

REFERENCES

Ammirati, J.B., Alvarado, P. & Beck, S., 2015. A lithospheric velocity model for the flat slab region of Argentina from joint inversion of Rayleigh wave phase velocity dispersion and teleseismic receiver functions, *Geophys. J. Int.,* **202,** 224–241.

Ammon, C., Randall, G.E. & Zandt, G., 1990. On the non-uniqueness of receiver function inversions, *J. geophys. Res.,* **95,** 15 303–15 318.

Aziz Zanjani, A., Zhu, L., Herrmann, R.B., Liu, Y., Gu, Z. & Conder, J.A., 2019. Crustal structure beneath the Wabash Valley Seismic Zone from the joint inversion of receiver functions and surface-wave dispersion: implications for continental rifts and intraplate seismicity, *J. geophys. Res.,* **124**(7), 7028–7039.

Bao, X. *et al.*, 2015. Two crustal low-velocity channels beneath SE Tibet revealed by joint inversion of Rayleigh wave dispersion and receiver functions, *Earth planet. Sci. Lett.,* **415,** 16–24.

Berteussen, K.A., 1977. Moho depth determinations based on spectral-ratio analysis of NORSAR long-period P waves, *Phys. Earth planet. Inter.,* **15,** 13–27.

Braile, L.W., Hinze, W.J., Keller, G.R. & Lidiak, E.G., 1986. Tectonic development of the New Madrid Rift Complex, Mississippi Embayment, North America, *Tectonophysics,* **131,** 1–21.

Chang, S.J. & Baag, C.E., 2005. Crustal structure in southern Korea from joint analysis of teleseismic receiver functions and surface-wave dispersion, *Bull. seism. Soc. Am.,* **95,** 1,516–1,534.

Chang, S.J., Baag, C.E. & Langston, C.A., 2004. Joint analysis of teleseismic receiver functions and surface wave dispersion using the genetic algorithm, *Bull. seism. Soc. Am.,* **94,** 691–704.

Christensen, N.I., 1996. Poisson's ratio and crustal seismology, *J. geophys. Res.,* **101,** 3139–3156.

Du, Z.J. & Foulger, G.R., 1999. The crustal structure beneath the northwest fjords, Iceland, from receiver functions and surface waves, *Geophys. J. Int.,* **139,** 419–432.

Ervin, C.P. & McGinnis, L.D., 1975. Reelfoot rift: reactivated precursor to the Mississippi embayment, *Geol. Soc. Am. Bull.,* **86,** 1287–1295.

Gilligan, A., Roecker, S.W., Priestley, K.F. & Nunn, C., 2014. Shear velocity model for the Kyrgyz Tien Shan from joint inversion of receiver function and surface wave data, *Geophys. J. Int.,* **199,** 480–498.

Hamburger, M.W. & Rupp, J.A., 1988. The June 1987 southeastern Illinois earthquake: possible tectonism associated with the La Salle Anticlinal Belt, *Seismol. Res. Lett.,* **59,** 151–157.

Haskell, N.A., 1964. Radiation pattern of surface waves from point sources in a multi-layered medium, *Bull. seism. Soc. Am.,* **54,** 377–393.

Herrmann, R.B., 2013. Computer programs in seismology: an evolving tool for instruction and research, *Seismol. Res. Lett.,* **84,** 1081–1088.

Herrmann, R.B., Withers, M. & Benz, H., 2008. The April 18, 2008 Illinois earthquake: an ANSS monitoring success, *Seismol. Res. Lett.,* **79,** 830–843.

Horspool, N.A., Savage, M.K. & Bannister, S., 2006. Implications for intraplate volcanism and back-arc deformation in northwestern New Zealand, from joint inversion of receiver functions and surface waves, *Geophys. J. Int.,* **166,** 1466–1483.

Julia, J., Ammon, C.J., Herrmann, R.B. & Correig, A.M., 2000. Joint inversion of receiver function and surface wave dispersion observations, *Geophys. J. Int.,* **143,** 99–112.

Julià, J., Ammon, C.J. & Herrmann, R.B., 2003. Lithospheric structure of the Arabian Shield from the joint inversion of receiver functions and surface-wave group velocities, *Tectonophysics,* **371,** 1–21.

Julià, J., Ammon, C.J. & Nyblade, A.A., 2005. Evidence for mafic lower crust in Tanzania, East Africa, from joint inversion of receiver functions and Rayleigh wave dispersion velocities, *Geophys. J. Int.,* **162,** 555–569.

Kim, W.Y., 2003. The 18 June 2002 Caborn, Indiana, earthquake: reactivation of ancient rift in the Wabash Valley Seismic Zone?, *Bull. seism. Soc. Am.,* **95,** 2201–2211.

Lai, C.G., Foti, S. & Rix, G.J., 2005. Propagation of data uncertainty in surface wave inversion, *JEEG,* **10,** 219–228.

Langston, C.A., 1979. Structure under Mount Rainier, Washington, inferred from teleseismic body waves, *J. geophys. Res.,* **84,** 4749–4762.

Last, R.J., Nyblade, A.A. & Langston, C.A., 1997. Crustal structure of the East African Plateau from receiver functions and Rayleigh wave phase velocities, *J. geophys. Res.,* **102,** 24 469–24 483.

Lawson, C.L. & Hanson, D.J., 1974. *Solving Least Squares Problems,* Prentice-Hall.

Ma, X. & Lowry, A., 1997. USArray imaging of continental crust in the conterminous United States, *Tetctonics,* **36,** 2882–2902.

McEvilly, T.V., 1964. Central U.S. crust-upper mantle structure from Love and Rayleigh wave phase velocity inversion, *Bull. seism. Soc. Am.,* **54,** 1997–2015.

Menke, W., 2012. *Geophysical Data Analysis: Discrete Inverse Theory,* Academic Press.

Mooney, W.D., Andrews, M.C., Ginzburg, A., Peters, D.A. & Hamilton, R.M., 1983. Crustal structure of the northern Mississippi embayment and a comparison with other continental rift zones, *Tectonophysics,* **94,** 327–348.

Nuttli, O.W., 1973. The Mississippi Valley earthquakes of 1811 and 1812: intensities, ground motion and magnitudes, *Bull. seism. Soc. Am.,* **63,** 227–248.

Obermeier, S.F., 1998. Liquefaction evidence for strong earthquakes of holocene and latest Pleistocene ages in the states of Indiana and Illinois, *Geology,* **50,** 227–254.

Owens, T.J., Zandt, G. & Taylor, S.R., 1984. Seismic evidence for ancient rift beneath the Cumberland plateau, Tennessee: a detailed analysis of broadband teleseismic *P* waveforms, *J. geophys. Res.,* **89,** 7783–7795.

Özalaybey, S., Savage, M.K., Sheehan, A.F., Louie, J.N. & Brune, J.N., 1997. Shear-wave velocity structure in the northern Basin and Range province from the combined analysis of receiver functions and surface waves, *Bull. seism. Soc. Am.,* **87,** 183–199.

Pond, E.C. & Martin, J.R., 1997. Estimated magnitudes and accelerations associated with prehistoric earthquakes in the Wabash Valley region of the central U.S., *Seismol. Res. Lett.,* **68,** 611–623.

Sambridge, M., 1999. Geophysical inversion with a neighbourhood algorithm - II. Appraising the ensemble, *Geophys. J. Int.,* **138,** 727–746.

Shen, W., Ritzwoller, M.H., Schulte-Pelkum, V. & Lin, F.C., 2012. Joint inversion of surface wave dispersion and receiver functions: a Bayesian Monte-Carlo approach, *Geophys. J. Int.,* **192,** 807–836.

Stauder, W. & Nuttli, O.W., 1970. Seismic studies: south central Illinois earthquake of November 9, 1968, *Bull. seism. Soc. Am.,* **60,** 973–981.

Tokam, K., Tabod, C.T., Nyblade, A.A., Julià, J., Wiens, D.A. & Pasyanos, M.E., 2010. Structure of the crust beneath Cameroon, West Africa, from the joint inversion of Rayleigh wave group velocities and receiver functions, *Geophys. J. Int.,* **183,** 1061–1076.

Xu, Z.J., Song, X. & Zhu, L., 2013. Crustal and uppermost mantle S velocity structure under Hi-CLIMB seismic array in central Tibetan Plateau from joint inversion of surface wave dispersion and receiver function data, *Tectonophysics,* **584,** 209–220.

Yang, H., Zhu, L. & Chu, R., 2009. Fault plane determination of the April 18, 2008 Mt. Carmel, Illinois, earthquake by detecting and relocating aftershocks, *Bull. seism. Soc. Am.,* **99(6),** 3413–3420.

Yoo, H.J., Herrmann, R.B., Cho, K.H. & Lee, K., 2007. Imaging the three-dimensional crust of the Korean peninsula by joint inversion of surface-wave dispersion and teleseismic receiver functions, *Bull. Seismol. Soc. Am.,* **97,** 1002–1011.

Zandt, G. & Ammon, C.J., 1995. Continental-crust composition constrained by measurements of crustal Poissons ratio, *Nature,* **374,** 152–154.

Zhu, L. & Kanamori, H., 2000. Moho depth variation in southern California from teleseismic receiver functions, *J. geophys. Res.,* **105,** 2969–2980.

Zhu, L. & Liu, Y., 2020. Measuring *PmP* traveltimes using teleseismic *S*-wave waveform data, *Earthq. Sciences,* **33,** 201–207.

APPENDIX: TRAVELTIMES AND THEIR DERIVATIVES

The forward calculation of the *Ps* delay time from interface *k* and the *PmP* traveltime (not including the horizontal distance contribution *px*) can be written as

$$t_{Ps}^{k} = \sum_{i=1}^{k} \sum_{j=1}^{n_i} (\eta_{ij}^{\beta} - \eta_{ij}^{\alpha}) h_i, \tag{A1}$$

$$t_{PmP} = 2 \sum_{i=1}^{k_{\text{Moho}}} \sum_{j=1}^{n_i} \eta_{ij}^{\alpha} h_i, \tag{A2}$$

where h_i is the sublayer thickness within the *i*th layer, and η_{ij}^{β} and η_{ij}^{α} are the vertical slownesses of the *S* and *P* waves in the *j*th sublayer of the *i*th layer, respectively,

$$\eta_{ij}^{\beta} = \sqrt{\frac{1}{{\beta_{ij}}^2} - p^2}, \tag{A3}$$

$$\eta_{ij}^{\alpha} = \sqrt{\frac{1}{{\beta_{ij}}^2 \kappa_i^2} - p^2}, \tag{A4}$$

and p is the horizontal slowness. The partial derivatives of t_{Ps}^{k} with respect to thickness, *S*-wave velocity, and *Vp*/*Vs* ratio of the *i*th layer ($i \le k$) are

$$\frac{\partial t_{Ps}^{k}}{\partial H_i} = \frac{1}{n_i} \sum_{j=1}^{n_i} \left(\eta_{ij}^{\beta} - \eta_{ij}^{\alpha} \right), \tag{A5}$$

$$\frac{\partial t_{Ps}^{k}}{\partial \beta_{ij}} = \frac{H_i}{n_i \beta_{ij}^3} \left(\frac{1}{\eta_{ij}^{\alpha} \kappa_i^2} - \frac{1}{\eta_{ij}^{\beta}} \right), \tag{A6}$$

$$\frac{\partial t_{Ps}^{k}}{\partial \kappa_i} = \frac{H_i}{n_i \kappa_i^3} \sum_{j=1}^{n_i} \frac{1}{\eta_{ij}^{\alpha} \beta_{ij}^2}. \tag{A7}$$

The partial derivatives of t_{PmP} with respect to thickness, *S*-wave velocity and *Vp*/*Vs* ratio of the *i*-layer ($i \le k$) are

$$\frac{\partial t_{PmP}}{\partial H_i} = \frac{2}{n_i} \sum_{j=1}^{n_i} \eta_{ij}^{\alpha}, \tag{A8}$$

$$\frac{\partial t_{PmP}}{\partial \beta_{ij}} = -\frac{2 H_i}{n_i \kappa_i^2 \beta_{ij}^3 \eta_{ij}^{\alpha}}, \tag{A9}$$

$$\frac{\partial t_{PmP}}{\partial \kappa_i} = -\frac{2 H_i}{n_i \kappa_i^3} \sum_{j=1}^{n_i} \frac{1}{\beta_{ij}^2 \eta_{ij}^{\alpha}}. \tag{A10}$$